



Room-temperature preparation of MIL-68 and its derivative In_2S_3 for enhanced photocatalytic Cr(VI) reduction and organic pollutant degradation under visible light

Huifen Fu, Lin Wu, Jing Hang, Peng Wang, Chen Zhao, Chong-Chen Wang*

Beijing Key Laboratory of Functional Materials for Building Structure and Environment Remediation, Beijing Advanced Innovation Centre for Future Urban Design, Beijing University of Civil Engineering and Architecture, Beijing, 100044, China

ARTICLE INFO

Article history:

Received 28 January 2020

Received in revised form

10 April 2020

Accepted 8 May 2020

Available online xxx

Keywords:

MIL-68

In_2S_3

Photocatalysis

ABSTRACT

MIL-68, a typical In-based MOF, has been studied in many fields due to its excellent performance. Facile preparation of MIL-68, suitable for scalable preparation and industrial applications, is of great significance. In this work, a method for the room-temperature preparation of rod-like MIL-68 at the nano- and micro-scales was developed for the first time, in which water or salts such as NaF, sodium formate, sodium acetate and sodium propionate were used as modulating reagents. It appears that these modulating reagents can promote the deprotonation of terephthalic acid and the hydrolysis of indium salt to accelerate crystal nucleation. The size of MIL-68 can be controlled by changing the modulating reagents. Hollow porous In_2S_3 particles composed of assembled ultrathin nanosheets were obtained via sulfidation treatment using MIL-68 as a self-sacrifice template, and the obtained In_2S_3 exhibited excellent photocatalytic activity toward Cr(VI) reduction and methyl orange degradation under LED visible light irradiation. Furthermore, the photocatalytic mechanism and reusability were studied.

© 2020 Elsevier B.V. All rights reserved.

1. Introduction

The problem of organic pollutants and heavy metals in water has attracted worldwide attention because these pollutants are a great source of risk to human well-being [1,2]. Photocatalysis, a sustainable technology using sunlight as an energy source, is a potential technology to remove pollutants from water [3,4]. However, developing advanced photocatalysts with excellent performance remains a challenge. Porous materials are becoming a hot topic in photocatalysis due to their abundant pores, large specific surface areas and many active sites, which could facilitate improvement of photocatalytic activity [5–7]. The hard-template method is a common strategy to synthesize porous materials [8–10], and this method has the disadvantage of frequently requiring multiple complicated steps.

Metal-organic frameworks (MOFs), a kind of porous crystalline material constructed from metal ions/clusters and organic linkers, possess great advantages such as porosity and tunable chemical functionality. MOFs have drawn great attention in many fields

[11–13], such as photocatalysis [14,15], adsorption [16,17], gas separation and storage [18,19]. Some MOFs are reported to display outstanding photocatalytic performance; however, there are some limitations to be overcome. First, most MOFs possess micropores, not mesopores, which are not useful in approaches targeting pollutants, especially organic pollutants with large sizes. Second, the stability of most MOFs in water is poor, which could cause secondary pollution because MOFs are built from organic ligands.

The adoption of MOFs as self-sacrificing templates to construct porous derivatives has received widespread attention [20,21]. For example, Li's group [22] successfully prepared Pt–ZnO– Co_3O_4 , Pt–ZnS–CoS and Pt–Zn₃P₂–CoP nanocomposites using ZnCo-ZIF particles as precursors, and these composites presented excellent performance toward photocatalytic hydrogen generation. However, MOFs are generally prepared using the hydrothermal/solvothermal method [23–25], in which some unique reactors are needed, and this method is not conducive to large-scale and high-throughput production. There is a very urgent need to find an inexpensive preparation method that can be implemented at room temperature to facilitate scalable preparation and commercial applications of MOFs.

MIL-68, a typical In-based MOF built from In^{3+} and terephthalic

* Corresponding author.

E-mail address: chongchenwang@126.com (C.-C. Wang).

acid (H₂BDC), has been widely investigated in many fields [26,27]. By using the solvothermal method, Wu's group [28] prepared NH₂-mediated MIL-68 particles which exhibited considerable activity for Cr(VI) reduction. Cheng's group [29] prepared MIL-68-NH₂/graphene oxide composite with good photocatalytic activity toward amoxicillin degradation. Currently, the derivatives of MIL-68 have received increasing attention [30]. For example, Wang's group [31] prepared tube-like In₂O₃/Co₃O₄ using Co^{II}-impregnated MIL-68 as a template, which exhibited excellent sensing performance toward triethylamine. Fang and coworkers [32] fabricated hollow In₂S₃ by sulfidation of MIL-68, and the hollow In₂S₃ exhibited high photocatalytic activity for the degradation of tetracycline hydrochloride and methyl orange (MO). MIL-68 was always synthesized by a solvothermal method or oil bath at a relatively high temperature (>90 °C) [32,33]. To the best of our knowledge, no room-temperature preparation method for MIL-68 has been reported. In this work, rod-like MIL-68 at the nano- and micro-scales was prepared at room temperature using H₂O or salts such as NaF, sodium formate, sodium acetate and sodium propionate as modulating reagents. This method is good for the scalable preparation and commercial applications of MIL-68, and we believe that this preparation strategy can be applied to other MOFs. Furthermore, porous In₂S₃ was obtained using MIL-68 as a self-sacrificing template, and the as-prepared In₂S₃ exhibited excellent photocatalytic activity toward Cr(VI) reduction and MO degradation under visible light.

2. Experimental section

2.1. Materials

All chemicals were commercially available and used without further purification. In(NO₃)₃·xH₂O and H₂BDC were purchased from Aladdin Reagent Co. Ltd. Thioacetamide (TAA) and *p*-benzoquinone (BQ) were purchased from J&K Scientific Ltd. NaF, sodium acetate and *t*-butanol (TBA) were purchased from Beijing Chemical Works. Sodium formate was purchased from Tianjin Guangfu Fine Chemical Industry Research Institute. Sodium propionate was purchased from Shanghai Sanaisi Reagent Co., Ltd.

2.2. Room-temperature preparation of MIL-68 using H₂O as the modulating reagent

H₂BDC (2 mmol) and In(NO₃)₃·xH₂O (2 mmol) were dissolved in 25 mL DMF and 5 mL H₂O, respectively. Subsequently, the aqueous solution of In(NO₃)₃·xH₂O was added to the DMF solution containing H₂BDC at room temperature under stirring. After 24 h, the precipitate was obtained after centrifugation and washed with ethanol twice.

2.3. Room-temperature preparation of MIL-68 using salts as modulating reagents

NaF was added to 25 mL DMF containing 2 mmol H₂BDC. Subsequently, 5 mL DMF containing 2 mmol In(NO₃)₃·xH₂O was added under stirring. After 24 h, a precipitate was obtained after centrifugation and washed twice with ethanol. The targeted products can also be obtained when NaF is replaced by sodium formate, sodium acetate and sodium propionate.

2.4. Preparation of porous hollow In₂S₃

First, 0.5 g as-prepared MIL-68 was dispersed in 75 mL ethanol containing 2 g TAA, which was transferred to a 100 mL Teflon-lined stainless-steel Parr bomb and heated at 120 °C for 8 h. After cooling to room temperature, porous hollow In₂S₃ was obtained. The In₂S₃

particles derived from MIL-68 prepared using H₂O, sodium formate, sodium acetate, sodium propionate and NaF as modulating reagents were named S1, S2, S3, S4 and S5, respectively.

2.5. Characterization

X-ray diffraction (XRD) patterns were recorded on a Dandong-haoyuan DX-2700B diffractometer using Cu K α radiation. The morphologies of the samples were observed using scanning electron microscopy (SEM, SU8020), transmission electron microscopy (TEM, JEM1200EX) and high-resolution transmission electron microscopy (HRTEM, FEI Tecnai G2 F30). Textural characteristics and specific surface areas were characterized using an ASAP 2460 analyzer. The UV–Vis diffuse-reflectance spectra (UV–Vis DRS) were obtained on a PerkinElmer Lambda 650S spectrometer. Electron spin resonance (ESR) signals of the radicals trapped by 5,5'-dimethyl-1-pyrroline N-oxide (DMPO) were detected using a JEOL JES-FA200 spectrometer. Mott-Schottky plots were measured on a Metrohm Autolab PGSTAT204 electrochemical workstation using a three-electrode system with In₂S₃-coated FTO glass, Pt plate and Ag/AgCl as the working electrode, counter electrode and reference electrode, respectively.

2.6. Photocatalytic experiment

First, the pH of the treated Cr(VI) solution was adjusted to 6.0. Then, 10 mg as-prepared In₂S₃ was dispersed in 50 mL Cr(VI) solution with the help of ultrasonication. After stirring in the dark for 1 h to achieve adsorption-desorption equilibrium, the suspension was irradiated under a 350 mW LED visible light source (PCX50A, Beijing Perfect Light Technology Co., Ltd.). At a set interval, 1.5 mL solution was removed and centrifuged, and the clear supernatant was measured by the diphenylcarbazide method using Auto Analyzer 3 (Seal, Germany). The process of MO photodegradation is similar to that of Cr(VI) photoreduction, and the residual MO concentration was determined on a Laspec Alpha-1860 UV–Vis spectrometer.

3. Results and discussion

MIL-68 was always prepared using In(NO₃)₃ and H₂BDC as precursors and DMF as the solvent via an oil bath or solvothermal routine [32,33]. In this study, rod-like MIL-68 was obtained at room temperature by adopting a DMF/H₂O (V/V, 25/5) mixture as the solvent (Fig. 1a–b). However, no significant precipitate was obtained when only DMF was used as the solvent, indicating that H₂O might trigger the reaction between In(NO₃)₃ and H₂BDC at room temperature. Additionally, to produce MIL-68 at room temperature, a DMF/H₂O mixture rather than H₂O alone was used as the solvent because H₂BDC cannot be sufficiently dissolved in water. It can be seen from Fig. 1b that the prepared MIL-68 presented a rod-like shape, which was similar to the MIL-68 prepared using the reported method at 90 °C (Fig. S1). This revealed that H₂O could accelerate the formation of MIL-68 and exert a minor influence on its morphology and size. Wang's group [34] reported that a series of zirconium-metalloporphyrinic MOFs were successfully synthesized by introducing H₂O and monocarboxylic acid as modulating reagents, in which H₂O was considered to accelerate the hydrolysis of zirconium salt and facilitate the deprotonation of acid to promote crystal nucleation. Subsequently, they synthesized zirconium- and hafnium-based MOF nanocrystals under mild conditions in the presence of water and acetic acid [35]. In our case, it appears that H₂O can promote the deprotonation of terephthalic acid and the hydrolysis of indium salt to accelerate crystal nucleation. Considering that the formula of MIL-68 is In(OH) (O₂C–C₆H₄–CO₂)·

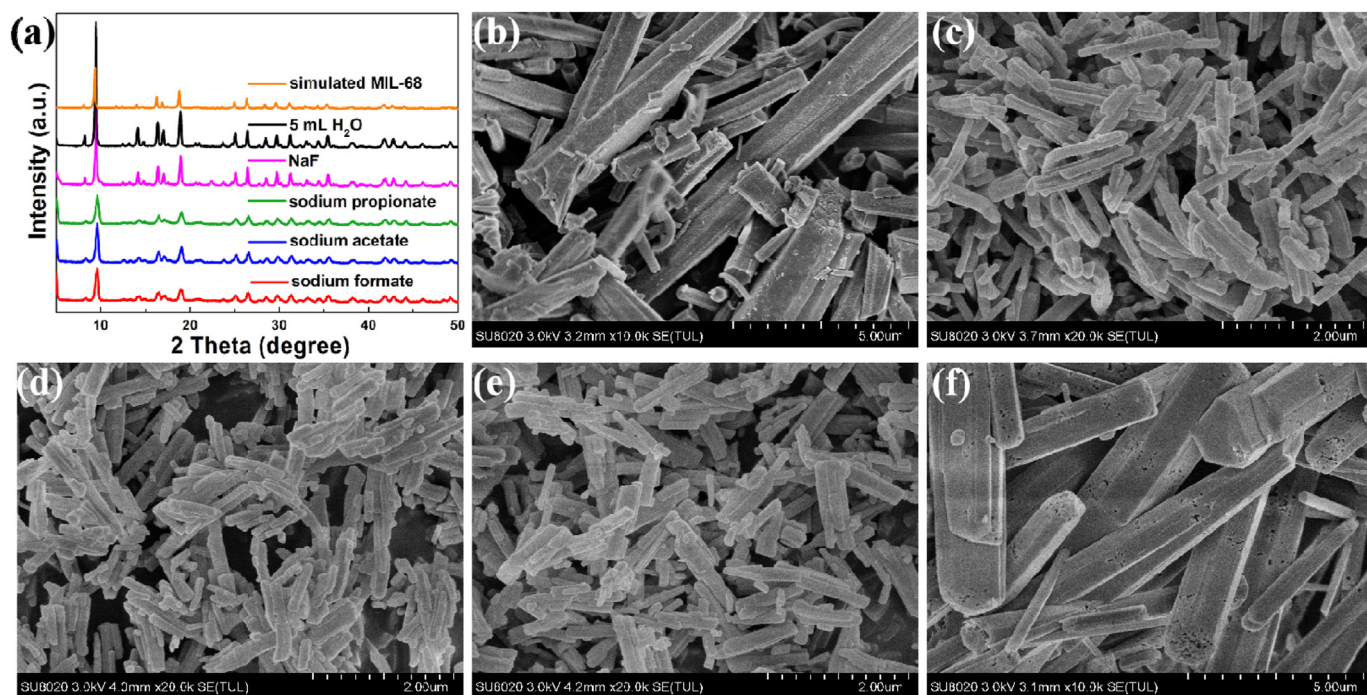


Fig. 1. (a) XRD patterns and (b–f) SEM images of MIL-68 prepared with the aid of (b) H₂O, (c) sodium formate, (d) sodium acetate, (e) sodium propionate and (f) NaF.

1.0DMF·zH₂O [36], it can be speculated that H₂O can facilitate the combination of In³⁺ and OH[−] and further promote the formation of MIL-68.

As depicted in Fig. 1a–f, rod-like MIL-68 was successfully prepared using only DMF as the solvent at room temperature when NaF was added as the modulating reagent, indicating that NaF can also result in the quick formation of MIL-68 at room temperature. It could be speculated that F[−] could promote the deprotonation of

H₂BDC to form BDC^{2−} (O₂C–C₆H₄–CO₂[−]) and further accelerate the reaction between In³⁺ and BDC^{2−}. It was reported that DMF can be decomposed under solvothermal conditions to yield dimethylamine, which acts as a Brønsted base, leading to the deprotonation of H₂BDC or H₃BTc and finally resulting in the formation of metal-BDC or metal-BTC composites [37,38]. At room temperature, H₂BDC cannot be deprotonated by DMF alone, while the addition of NaF promoted the deprotonation of H₂BDC, accelerating the formation

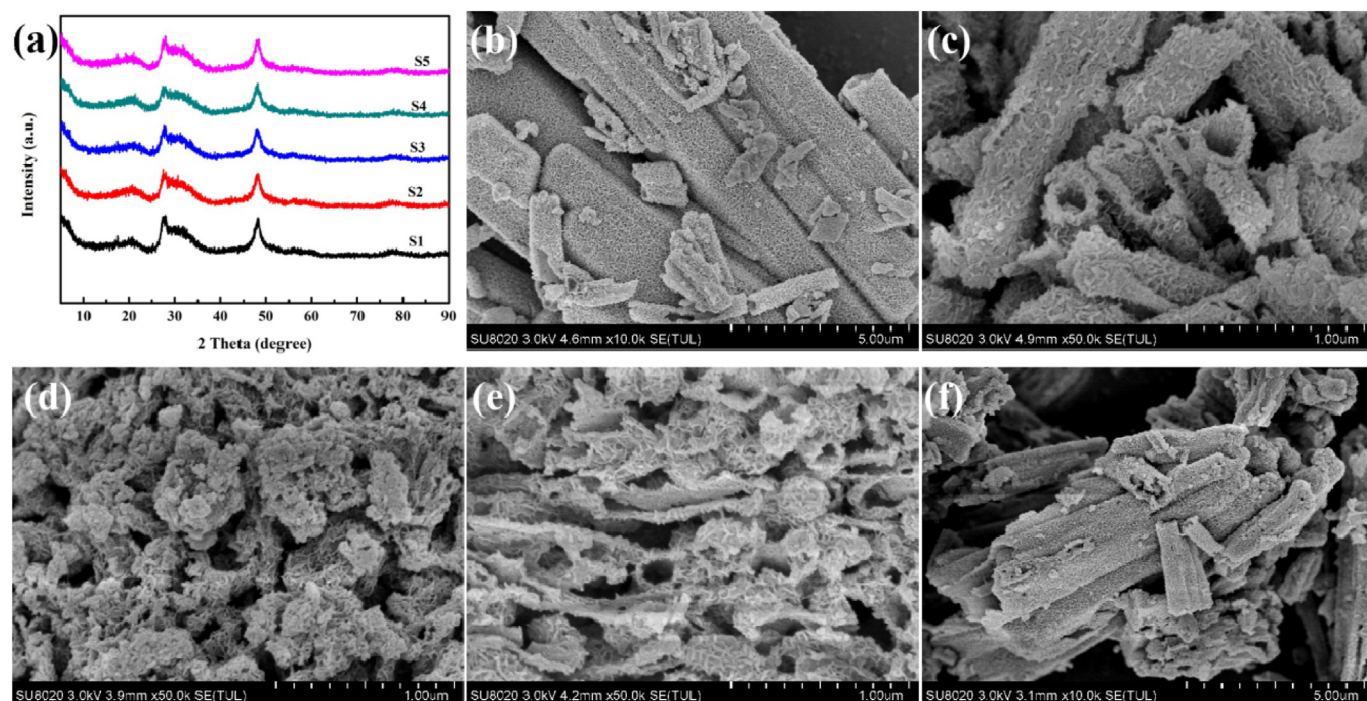


Fig. 2. (a) XRD patterns of S1, S2, S3, S4 and S5. SEM images of (b) S1, (c) S2, (d) S3, (e) S4 and (f) S5.

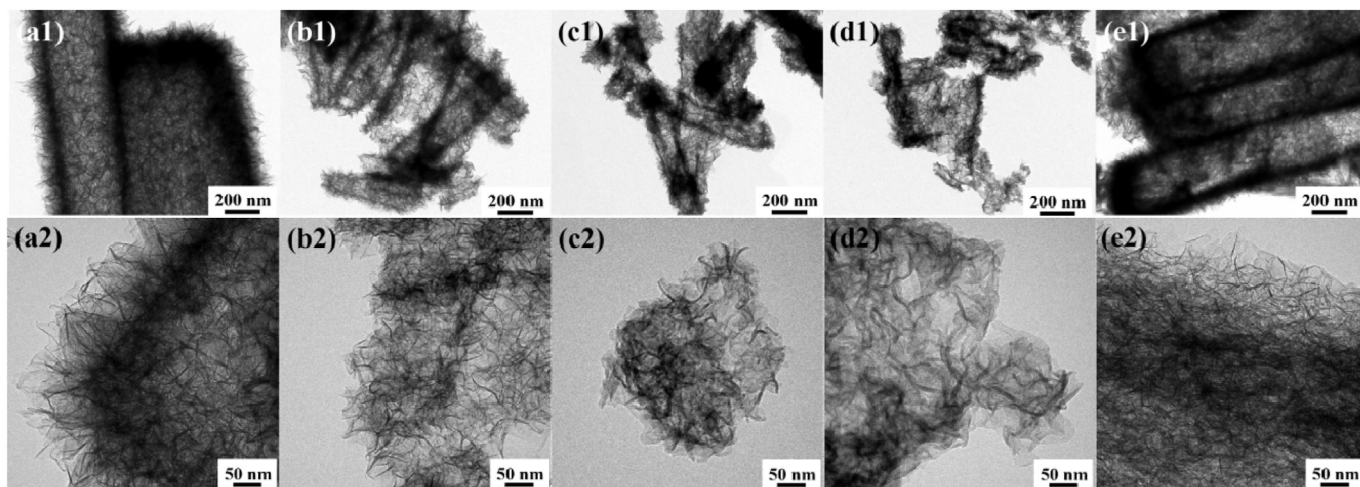


Fig. 3. TEM and HRTEM images of (a) S1, (b) S2, (c) S3, (d) S4 and (e) S5.

of MIL-68. Therefore, MIL-68 can be obtained under mild conditions at room temperature with the help of NaF. As shown in Fig. 1a, all diffraction peaks of MIL-68 prepared in the presence of NaF matched well with the simulated results [36], implying that F^- could not influence the coordination environment of In^{3+} in MIL-68. This was further confirmed by EDS determination, in which no F was detected in MIL-68 (Fig. S2).

In addition to NaF, three other alkali salts, sodium formate, sodium acetate and sodium propionate, were selected as modulating reagents to prepare MIL-68 at room temperature. It can be observed from Fig. 1a–1c–1e that rod-like MIL-68 materials were also obtained, which affirmed that these salts played important roles in the room-temperature synthesis. It is worth noting that the sizes of the three MIL-68 prepared in the presence of sodium formate, sodium acetate, and sodium propionate were smaller than the size of the MIL-68 prepared with the help of NaF, which may be attributed to the carboxyl group ($-COOH$) in the three modulating reagents (sodium formate, sodium acetate, sodium propionate) bonding on the specific surface of MIL-68, hindering the growth of the crystal plane and leading to the smaller size [39]. This room-temperature preparation of MIL-68 can be facily accomplished in beakers rather than special reactors, such as high-temperature and high-pressure reactors, and large-scale synthesis can be easily realized by using larger beakers or other general reactors,

which is imperative to advance the development of MIL-68.

As shown in Fig. 2a, the perfect match of characteristic XRD peaks of In_2S_3 and the absence of XRD peaks of MIL-68 revealed that these MIL-68 particles were completely transformed into In_2S_3 . It can be seen from Fig. 2b–f and Fig. 3 that all In_2S_3 exhibited hollow structures. Moreover, all these In_2S_3 particles were composed of ultrathin

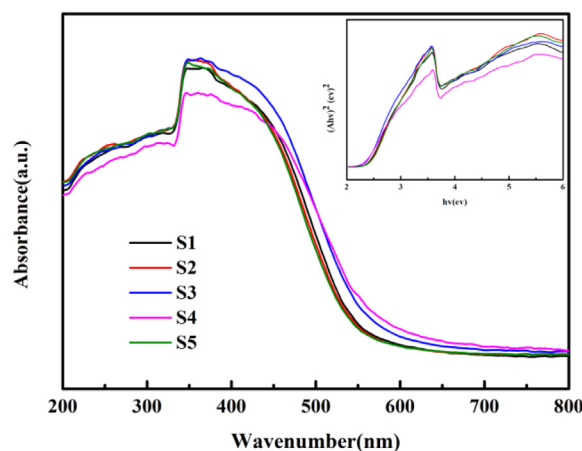


Fig. 5. UV-Vis spectra and plots of $(ah\nu)^2$ versus photoenergy of different In_2S_3 samples.

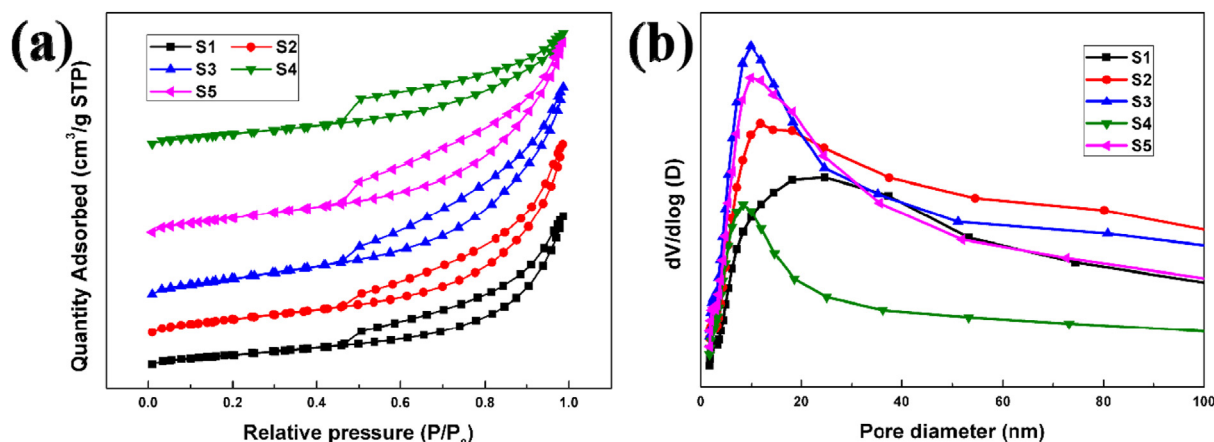


Fig. 4. (a) N_2 adsorption-desorption isotherms and (b) pore size diameter distributions of different as-prepared In_2S_3 samples.

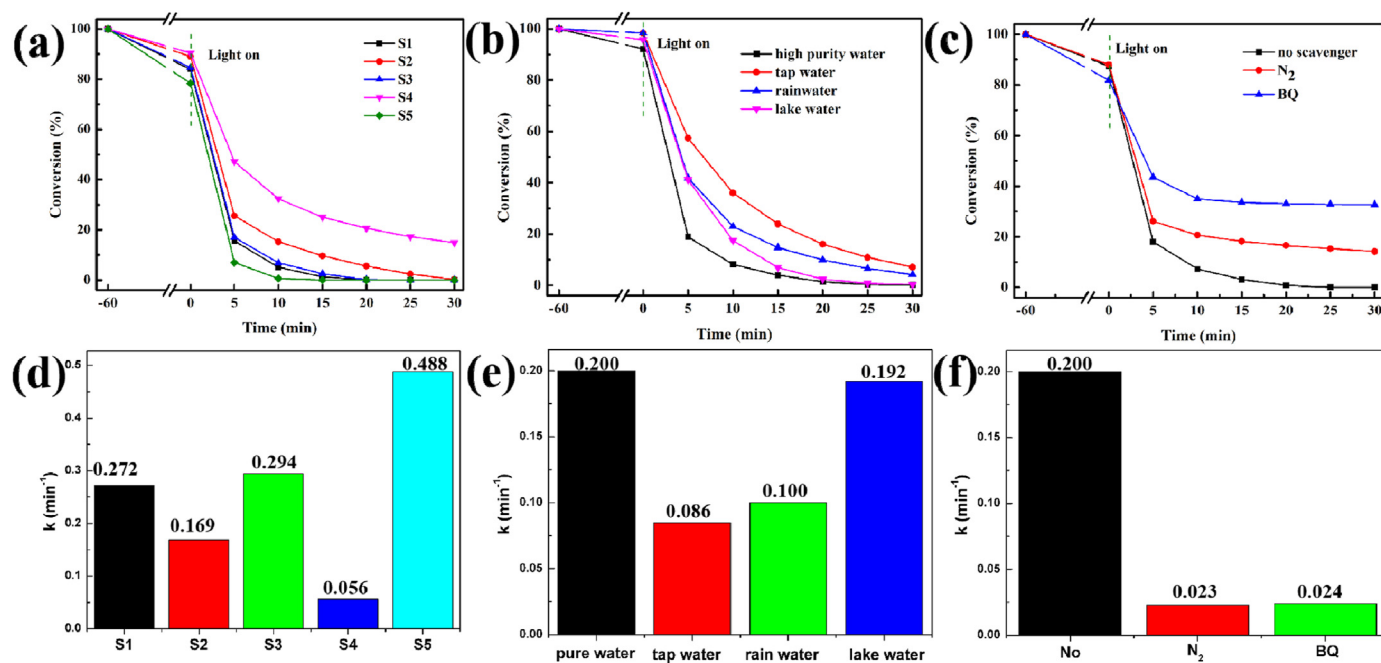


Fig. 6. (a) Photocatalytic conversion curves and (d) kinetic constants of different photocatalysts for Cr(VI) reduction. Reaction conditions: photocatalyst = 10 mg, Cr(VI) = 10 mg/L, 50 mL, pH = 6.0. (b) Photocatalytic conversion curves and (e) kinetic constants of S5 toward Cr(VI) reduction in lake/rain/tap/pure water system, (c) photocatalytic conversion curves and (f) kinetic constants of S5 toward Cr(VI) reduction in the presence of different scavengers. Reaction conditions: photocatalyst = 10 mg, Cr(VI) = 20 mg/L, 50 mL, pH = 6.0.

nanosheets, which was beneficial for increasing the specific surface area. During the formation process of In₂S₃, TAA may first react with the superficial In³⁺ of MIL-68 to form nanosheet-like In₂S₃ on the surface of MIL-68, producing an In₂S₃@MIL-68 core-shell structure. Then, BDC²⁻ ligands could be released and result in empty spaces originally occupied by BDC²⁻ in MIL-68. Subsequently, the In³⁺ inside would diffuse outward to react with TAA to form In₂S₃. Over time, porous hollow In₂S₃ particles composed of assembled ultrathin nanosheets were finally formed.

N₂ adsorption-desorption isotherms and pore size distributions are shown in Fig. 4. All In₂S₃ samples exhibited type IV N₂ adsorption-desorption isotherms, revealing the mesoporous structures [40]. The pore diameters of these In₂S₃ were distributed in a wide range from 2 nm to 50 nm. The specific surface areas of S1, S2, S3, S4 and S5 are 122.7, 170.4, 207.2, 133.9 and 186.9 m²/g, respectively, which are much higher than those of other In₂S₃ samples reported in the literature [41,42].

The optical properties were measured by UV-Vis DRS, and the E_g values were calculated according to Eq. (1).

$$ah\nu = K(h\nu - E_g)^{1/n} \quad (1)$$

where a , h , ν and K are the diffuse absorption coefficient, Plank constant, light frequency and a constant, respectively. n is determined by the type of optical transition of a semiconductor. For the direct bandgap of In₂S₃, the value of n is 2. It can be seen from Fig. 5 that the E_g values of S1, S2, S3, S4 and S5 are 2.41, 2.43, 2.38, 2.36 and 2.44 eV, respectively, indicating that these In₂S₃ could display photocatalytic performances under visible light.

The photocatalytic performances of these In₂S₃ toward Cr(VI) reduction at pH 6.0 were estimated under visible light irradiation. First, the adsorption abilities of In₂S₃ samples toward Cr(VI) were tested in the dark, and Fig. S3a shows that all the porous In₂S₃ photocatalysts accomplished <20% Cr(VI) removal after adsorption-

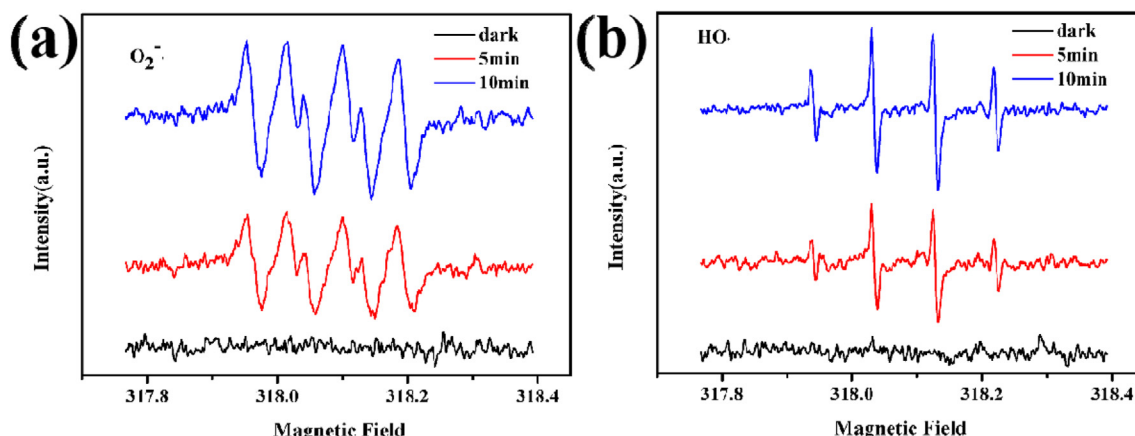


Fig. 7. ESR spectra of (a) •OH and (b) •O₂⁻ active radicals trapped by DMPO on S5.

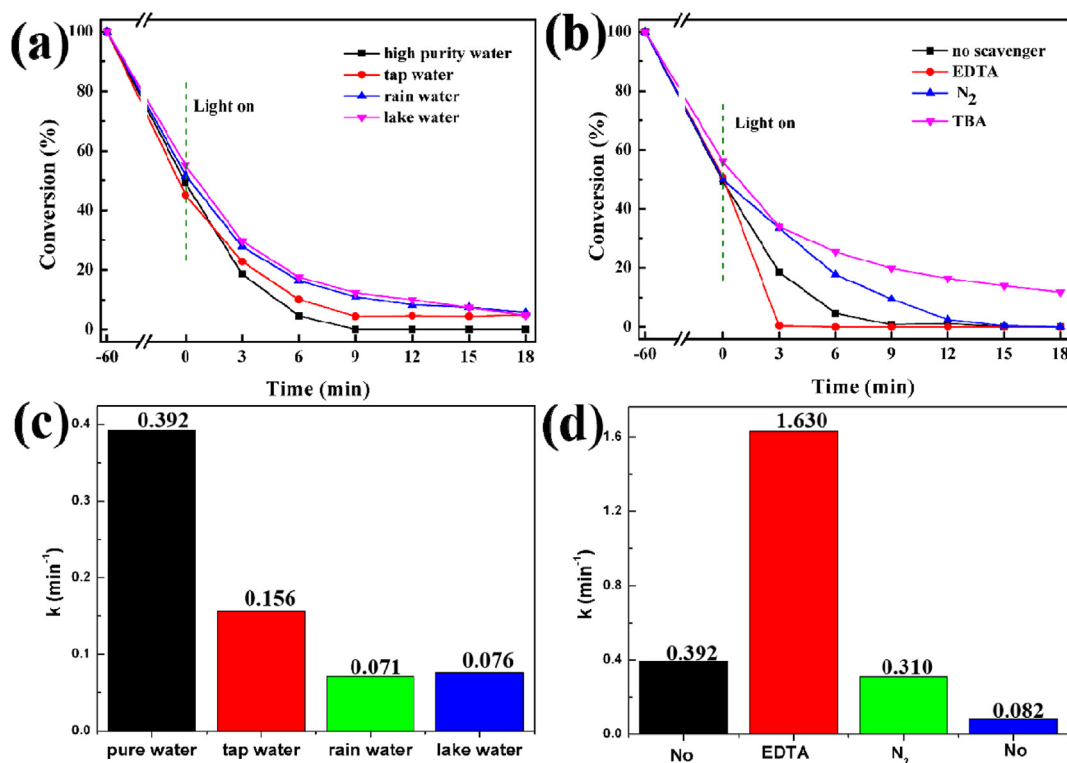


Fig. 8. (a) Photocatalytic conversion curves and (c) kinetic constants of S5 toward MO degradation in different systems, (b) photocatalytic conversion curves and (d) kinetic constants of S5 toward MO degradation in the presence of different scavengers. Reaction conditions: photocatalyst = 10 mg, MO = 10 mg/L, 50 mL.

desorption equilibrium within 1 h. The control experiment manifested that no obvious self-photoreduction was observed under visible light irradiation (Fig. S3b). However, nearly 100% Cr(VI) photoreduction efficiencies were achieved within 30 min with S1, S2, S3 and S5 as photocatalysts (Fig. 6a and d). S5 exhibited the best photocatalytic activity toward Cr(VI) reduction, followed by S1, S3, S2 and S4. As reported, the photoreduction activity of Cr(VI) decreased with increasing pH and generally reached its highest value at pH = 2 [43–45]. In our case, S5 achieved nearly 100% Cr(VI) reduction at pH 6.0. Cr(VI) reduction under neutral conditions is cost-saving and sustainable, as a lower pH would consume a considerable amount of acid, such as H₂SO₄ and HCl. Compared to the photocatalysts reported in the literature, S5 presented superior photocatalytic performance toward Cr(VI) reduction (Table S1) [46–51].

The initial Cr(VI) concentration can affect the photocatalytic performance. Fig. S4 shows that the photocatalytic activities decreased with increasing Cr(VI) concentration. To further investigate the photocatalytic performance and practical application of the obtained In₂S₃, a photocatalytic experiment was conducted in simulated wastewater samples containing Cr(VI) prepared with tap water, rainwater and lake water. As illustrated in Fig. 6b and e, slight decreases in the photoreduction of Cr(VI) in different natural water samples were observed, probably due to the inhibitory effect of coexisting ions such as Cl⁻, NO₃⁻, PO₄³⁻ and SO₄²⁻ in natural water [44]. For the three natural water systems, the photoreduction efficiencies of Cr(VI) in lake water and rainwater were superior to the photoreduction efficiency in tap water. It was determined that dissolved organic matter (DOM) existed in lake water and rainwater as organics could deplete h⁺, leading to the effective separation of photoinduced electron-hole pairs and the formation of more e⁻ or/and ·O₂⁻. Although the DOM in rainwater and lake water could consume h⁺, the inhibitory effects from the inorganic ions may outweigh the promotional effect from the DOM, leading to a lower

photoreduction efficiency in natural water than in ultrapure water. Moreover, the different photoreduction efficiencies in different natural water systems could be attributed to the different inhibitory effects and promotional effects.

It was reported that the active species for photocatalytic Cr(VI) reduction were generally e⁻ and ·O₂⁻ [52–55]. To understand the photocatalytic mechanism, BQ, a trapping agent of ·O₂⁻, was introduced during the photocatalytic process. As shown in Fig. 6c and f, the photocatalytic activity of S5 was inhibited with the addition of BQ, indicating that ·O₂⁻ played an important role in Cr(VI) reduction. N₂ was bubbled into the reaction system to remove dissolved oxygen (DO) and avoid the formation of ·O₂⁻. It can be seen from Fig. 6c that the photocatalytic activity was also

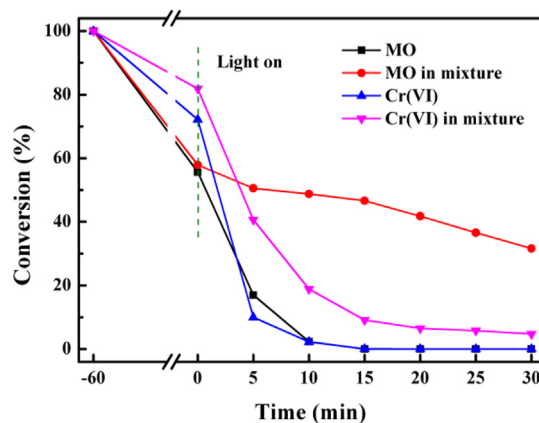


Fig. 9. Photocatalytic performance of Cr(VI) reduction and MO degradation over S5 in a single-component system and a mixed system. Reaction conditions: photocatalyst = 10 mg, MO = 10 mg/L, Cr(VI) = 20 mg/L, 50 mL.

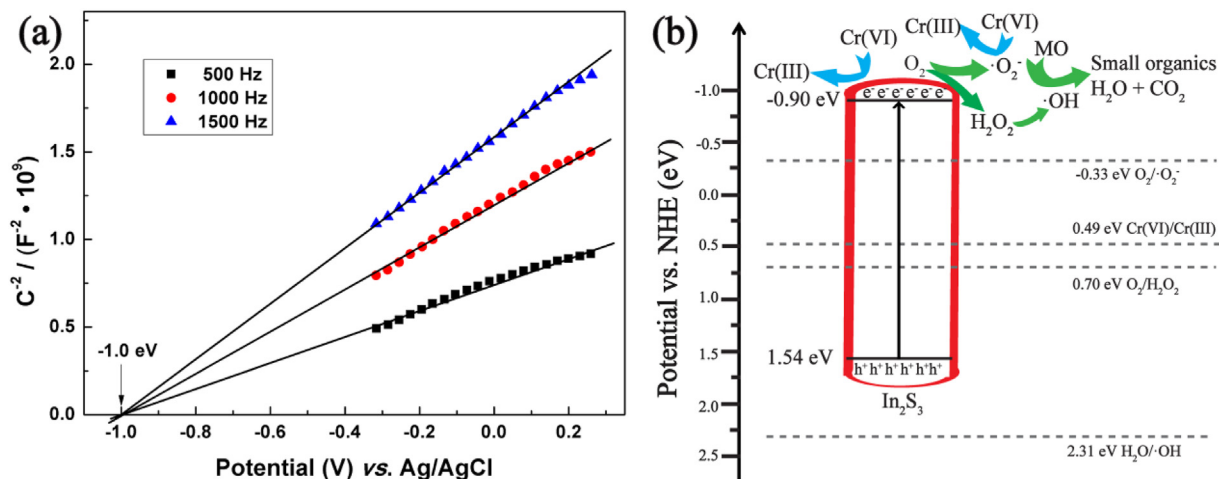


Fig. 10. (a) Mott-Schottky plots of S5 and (b) mechanism diagram of In_2S_3 for photocatalytic $Cr(VI)$ reduction and MO degradation.

restrained, further demonstrating that $\cdot O_2^-$ might be a main active species for $Cr(VI)$ reduction. In addition, the photoreduction of $Cr(VI)$ still occurred in the presence of BQ or with a bubble of N_2 , suggesting that e^- could also be significant for $Cr(VI)$ reduction.

Electron spin resonance (ESR) was performed to test whether $\cdot O_2^-$ radicals existed under visible light irradiation. Fig. 7a shows that there was no DMPO- $\cdot O_2^-$ signal in the dark. However, four intensive peak signals with a ratio of 1:1:1:1 occurred under visible light irradiation, and these peaks became stronger with time, indicating that more $\cdot O_2^-$ radicals were generated [56,57]. From the discussions above, it can be concluded that $\cdot O_2^-$ and e^- could be

responsible for the photoreduction of $Cr(VI)$.

The photocatalytic performance toward MO degradation over S5 was also studied. The saturation adsorption of MO with approximately 45% removal efficiency was achieved after 1 h in the dark (Fig. S5a). It can be seen from Fig. S5b that self-degradation was not obvious. Nearly 100% MO with an initial concentration of 10 mg/L was removed within 9 min upon irradiation with visible light (Fig. 8a). To prove the excellent photocatalytic performance, photocatalytic experiments were conducted in simulated wastewater samples containing MO prepared with lake water, rainwater and tap water. As exhibited in Fig. 8a, a slight decline in the photocatalytic

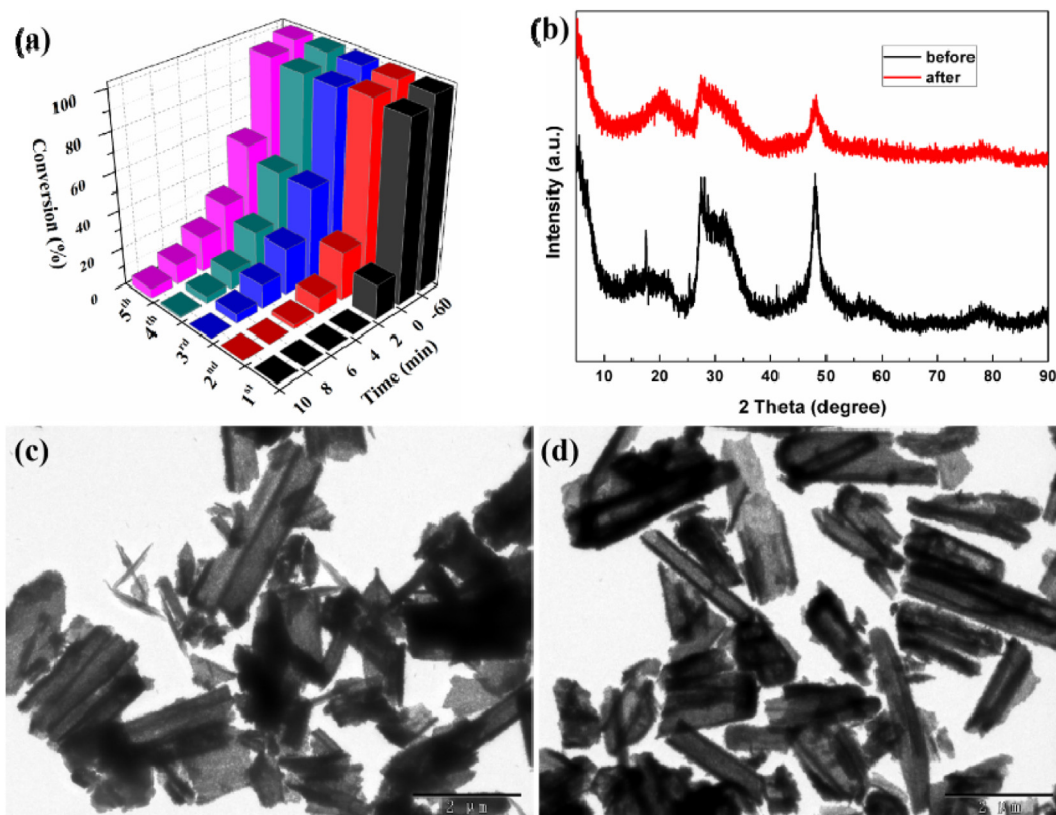


Fig. 11. (a) Reusability of S5 for the photoreduction of $Cr(VI)$, (b) XRD patterns, and (c, d) TEM images of S5 (c) before and (d) after catalysis.

activity was observed, and the conversion efficiency reached approximately 95% within 18 min. To understand the photocatalytic mechanism, TBA was introduced during the photocatalytic process to trap $\cdot\text{OH}$ radicals. It can be observed from Fig. 8b that the photodegradation efficiency was inhibited, implying that $\cdot\text{OH}$ could be responsible for the degradation of MO. The photocatalytic performance toward MO degradation was improved in the presence of EDTA acting as a h^+ trapping reagent, which could be attributed to the increased $\cdot\text{O}_2^-$ production upon separation of photoinduced electron-hole pairs. Furthermore, when N_2 was bubbled into the reaction system to remove DO , the photocatalytic activity was restrained, further implying that $\cdot\text{O}_2^-$ could also play an important role in the degradation of MO. The ESR results (Fig. 7b) showed that there was no DMPO- $\cdot\text{OH}$ signal in the dark, while four intensive peak signals with a ratio of 1:2:2:1 occurred under visible light irradiation. Furthermore, these four peaks became stronger with time, revealing that more $\cdot\text{OH}$ radicals were generated [58]. From the discussions above, it can be concluded that the dominant active species for MO photodegradation were $\cdot\text{O}_2^-$ and $\cdot\text{OH}$ radicals.

Considering that both Cr(VI) and organics can exist in real wastewater, the photocatalytic performances of Cr(VI) reduction and MO degradation in a mixed solution of Cr(VI) and MO were measured. It can be observed from Fig. 9 that the Cr(VI) photoreduction and MO photodegradation efficiencies in the mixed system both decreased compared to those in the single-component systems, which could be ascribed to the competitive consumption of $\cdot\text{O}_2^-$ between Cr(VI) reduction and MO degradation.

To further understand the photocatalytic mechanism, Mott-Schottky plots of S5 were measured. As shown in Fig. 10a, the flat band potential is -1.00 eV vs. Ag/AgCl . For In_2S_3 (n -type semiconductor), the minimum value of the CB is 0.1 eV higher than that of the flat band potential [59], and the CB value should be -1.10 eV vs. Ag/AgCl , which can be converted to -0.90 eV vs. NHE using Eq. (2). The E_g value is 2.44 eV, therefore the VB value is 1.54 eV.

$$E_{\text{NHE}} = E_{\text{Ag/AgCl}} + 0.2 \text{ eV} \quad (2)$$

The mechanism diagram is shown in Fig. 10b. In the photocatalytic reduction of Cr(VI) , the main active species were e^- and $\cdot\text{O}_2^-$, while $\cdot\text{OH}$ and $\cdot\text{O}_2^-$ were the main active species for the degradation of MO. $\cdot\text{O}_2^-$ was generated as described by Eq. (3), while $\cdot\text{OH}$ was formed as described by Eqs. (4) and (5) rather than by Eq. (6) because the VB potential of S5 was not positive enough to produce $\cdot\text{OH}$ [60].



Reusability is an important parameter for photocatalysts. As exhibited in Fig. 11a, the photoreduction efficiency toward 10 mg/L Cr(VI) could reach 95% within 10 min after five runs of operation. The XRD patterns and TEM images of S5 after catalysis were not obviously changed, as shown in Fig. 11b–d, indicating good stability of the obtained In_2S_3 .

4. Conclusion

In summary, a method for the room-temperature preparation of MIL-68 was developed using H_2O and salts such as NaF , sodium

formate, sodium acetate and sodium propionate as modulating reagents for the first time. H_2O could promote the hydrolysis of indium salt and the deprotonation of terephthalic acid to accelerate crystal nucleation, and the salts could also promote the deprotonation of terephthalic acid to accelerate the formation of MIL-68. This preparation method is suitable for large-scale production and industrial applications of MIL-68. Hollow porous In_2S_3 particles with assembled ultrathin nanosheets were obtained via sulfidation treatment using these MIL-68 as self-sacrificing templates. The obtained In_2S_3 possessed excellent photoreduction of Cr(VI) and photodegradation of MO. $\cdot\text{O}_2^-$ and e^- could be responsible for the photoreduction of Cr(VI) , and both $\cdot\text{O}_2^-$ and $\cdot\text{OH}$ were the dominant active species in the photodegradation of MO. Furthermore, the reusability of In_2S_3 was good, and there was no obvious decline in photocatalytic performance after five runs of operation.

Declaration of competing interest

The authors declare that they have no known competing financial interests or personal relationships that could have appeared to influence the work reported in this paper.

CRediT authorship contribution statement

Huifen Fu: Data curation, Investigation, Visualization, Writing - original draft. **Lin Wu:** Data curation, Methodology, Software. **Jing Hang:** Visualization, Software. **Peng Wang:** Resources. **Chen Zhao:** Validation, Software. **Chong-Chen Wang:** Conceptualization, Funding acquisition, Supervision, Project administration, Writing - review & editing.

Acknowledgements

This work was supported by the National Natural Science Foundation of China (21806008, 21876008, 51878023), Beijing Natural Science Foundation (8202016), Beijing Talent Project (2019A22), Great Wall Scholars Training Program Project of Beijing Municipality Universities (CIT&TCD20180323).

Appendix A. Supplementary data

Supplementary data to this article can be found online at <https://doi.org/10.1016/j.jallcom.2020.155567>.

References

- [1] H.-Y. Jing, T. Wen, C.-M. Fan, G.-Q. Gao, S.-L. Zhong, A.-W. Xu, Efficient adsorption/photodegradation of organic pollutants from aqueous systems using Cu_2O nanocrystals as a novel integrated photocatalytic adsorbent, *J. Mater. Chem.* 2 (2014) 14563–14570.
- [2] Y. Ge, Z. Li, Application of lignin and its derivatives in adsorption of heavy metal ions in water: a review, *ACS Sustain. Chem. Eng.* 6 (2018) 7181–7192.
- [3] Y.-C. Zhou, P. Wang, H. Fu, C. Zhao, C.-C. Wang, Ternary $\text{Ag/Ag}_3\text{PO}_4/\text{MIL-125-NH}_2$ Z-scheme heterojunction for boosted photocatalytic Cr(VI) cleanup under visible light, *Chin. Chem. Lett.* (2020), <https://doi.org/10.1016/j.cclet.2020.02.048>.
- [4] L. Mohapatra, K. Parida, A review on the recent progress, challenges and perspective of layered double hydroxides as promising photocatalysts, *J. Mater. Chem.* 4 (2016) 10744–10766.
- [5] J. Abdi, M. Yahyanezhad, S. Sakhaie, M. Vossoughi, I. Alemzadeh, Synthesis of porous $\text{TiO}_2/\text{ZrO}_2$ photocatalyst derived from zirconium metal organic framework for degradation of organic pollutants under visible light irradiation, *J. Environ. Chem. Eng.* 7 (2019), 103096.
- [6] S. Wang, B.Y. Guan, X.W. Lou, Construction of $\text{ZnIn}_2\text{S}_4\text{-In}_2\text{O}_3$ hierarchical tubular heterostructures for efficient CO_2 photoreduction, *J. Am. Chem. Soc.* 140 (2018) 5037–5040.
- [7] B. Zhang, J. Zhang, X. Tan, D. Shao, J. Shi, L. Zheng, G. Yang, B. Han, MIL-125- NH_2/TiO_2 core-shell particles produced by post-solvothermal route for high-performance photocatalytic H_2 production, *ACS Appl. Mater. Interfaces* 10 (2018) 16418–16423.
- [8] A. Lolli, R. Amadori, C. Lucarelli, M.G. Cutrufello, E. Rombi, F. Cavani,

- S. Albonetti, Hard-template preparation of Au/CeO₂ mesostructured catalysts and their activity for the selectivity oxidation of 5-hydroxymethylfurfural to 2,5-furandicarboxylic acid, *Microporous Mesoporous Mater.* 116 (2016) 266–475.
- [9] B. Ding, Y. Zhou, M. He, T. Huang, S. Li, S. Huang, W. Pan, Synthesis of a hollow CeO₂/Au/C hierarchical nanostructure for high catalytic activity and recyclability, *RSC Adv.* 6 (2016) 100427–100436.
- [10] Z. Wang, H. Fu, Z. Tian, D. Han, F. Gu, Strong metal-support interaction in novel core-shell Au-CeO₂ nanostructures induced by different pretreatment atmospheres and its influence on CO oxidation, *Nanoscale* 8 (2016) 5865–5872.
- [11] J. Liu, L. Chen, H. Cui, J. Zhang, L. Zhang, C.-Y. Su, Applications of metal-organic frameworks in heterogeneous supramolecular catalysis, *Chem. Soc. Rev.* 43 (2014) 6011–6061.
- [12] Q. Wang, D. Astruc, State of the art and prospects in Metal-Organic Framework (MOF)-based and MOF-derived nanocatalysis, *Chem. Rev.* 120 (2020) 1438–1511.
- [13] H. Fu, X.-X. Song, L. Wu, C. Zhao, P. Wang, C.-C. Wang, Room-temperature preparation of MIL-88A as a visible-light-driven photocatalyst for degradation of rhodamine B and bisphenol A, *Mater. Res. Bull.* 125 (2020), 110806.
- [14] Y.-C. Zhou, X.-Y. Xu, P. Wang, H. Fu, C. Zhao, C.-C. Wang, Facile fabrication and enhanced photocatalytic performance of visible light responsive UiO-66-NH₂/Ag₂CO₃ composite, *Chin. J. Catal.* 40 (2019) 1912–1923.
- [15] X.-H. Yi, S.-Q. Ma, X.-D. Du, C. Zhao, H. Fu, P. Wang, C.-C. Wang, The facile fabrication of 2D/3D Z-scheme g-C₃N₄/UiO-66 heterojunction with enhanced photocatalytic Cr(VI) reduction performance under white light, *Chem. Eng. J.* 375 (2019), 121944.
- [16] J.-J. Li, C.-C. Wang, H. Fu, J.-R. Cui, P. Xu, J. Guo, J.-R. Li, High-performance adsorption and separation of anionic dyes in water using a chemically stable graphene-like metal-organic framework, *Dalton Trans.* 46 (2017) 10197–10201.
- [17] H.W.B. Teo, A. Chakraborty, S. Kayal, Formic acid modulated (fam) aluminium fumarate MOF for improved isotherms and kinetics with water adsorption: cooling/heat pump applications, *Microporous Mesoporous Mater.* 272 (2018) 109–116.
- [18] R.-B. Lin, S. Xiang, H. Xing, W. Zhou, B. Chen, Exploration of porous metal-organic frameworks for gas separation and purification, *Coord. Chem. Rev.* 378 (2019) 87–103.
- [19] Y. He, W. Zhou, G. Qain, B. Chen, Methane storage in metal-organic frameworks, *Chem. Soc. Rev.* 43 (2014) 5657–5678.
- [20] C. Wang, J. Kim, J. Tang, M. Kim, H. Lim, V. Malgras, J. You, Q. Xu, J. Li, Y. Yamauchi, New strategies for novel MOF-derived carbon materials based on nanoarchitectures, *Inside Chem.* 6 (2020) 19–40.
- [21] Y. Zhang, J. Zhou, X. Chen, Q. Feng, W. Cai, MOF-derived C-doped ZnO composites for enhanced photocatalytic performance under visible light, *J. Alloys Compd.* 777 (2019) 109–118.
- [22] M. Lan, R.-M. Guo, Y. Dou, J. Zhou, A. Zhou, J.-R. Li, Fabrication of porous Pt-doping heterojunctions by using bimetallic MOF template for photocatalytic hydrogen generation, *Nano Energy* 33 (2017) 238–246.
- [23] J. Qiu, L. Yang, M. Li, J. Yao, Metal nanoparticles decorated MIL-125-NH₂ and MIL-125 for efficient photocatalysis, *Mater. Res. Bull.* 112 (2019) 297–306.
- [24] L. Ding, P. Shao, Y. Luo, X. Yin, S. Yu, L. Fang, L. Yang, J. Yang, X. Luo, Functionalization of UiO-66-NH₂ with rhodamine via amidation: towards a robust adsorbent with dual coordination sites for selective capture of Ag(I) from wastewater, *Chem. Eng. J.* 382 (2019), 123009.
- [25] Z. Xiu, M.H. Alfaruqi, J. Gim, J. Song, S. Kim, P.T. Duong, J.P. Baboo, V. Mathew, J. Kim, MOF-derived mesoporous anatase TiO₂ as anode material for lithium-ion batteries with high rate capability and long cycle stability, *J. Alloys Compd.* 674 (2016) 174–178.
- [26] C. Yang, S. Wu, J. Cheng, Y. Chen, Indium-based metal-organic framework/graphite oxide composite as an efficient adsorbent in the adsorption of rhodamine B from aqueous solution, *J. Alloys Compd.* 687 (2016) 804–812.
- [27] Y. Lv, R. Zhang, S. Zeng, K. Liu, S. Huang, Y. Liu, P. Xu, C. Lin, Y. Cheng, M. Liu, Removal of p-arsanilic acid by an amino-functionalized indium-based metal-organic framework: adsorption behavior and synergetic mechanism, *Chem. Eng. J.* 339 (2018) 359–368.
- [28] R. Liang, L. Shen, F. Jing, W. Wu, N. Qin, R. Lin, L. Wu, NH₂-mediated indium metal-organic framework as a novel visible-light-driven photocatalyst for reduction of the aqueous Cr(VI), *Appl. Catal. B Environ.* 162 (2015) 245–251.
- [29] C. Yang, X. You, J. Cheng, H. Zheng, Y. Chen, A novel visible-light-driven In-based MOF/graphene oxide composite photocatalyst with enhanced photocatalytic activity toward the degradation of amoxicillin, *Appl. Catal. B Environ.* 200 (2017) 673–680.
- [30] L. Jin, X. Zhao, X. Qian, S. Wang, X. Shen, M. Dong, Synthesis of porous In₂O₃/carbon composites derived from metal-organic frameworks for high performance Li-ion batteries, *Mater. Lett.* 199 (2017) 176–179.
- [31] S. Shi, F. Zhang, H. Lin, Q. Wang, E. Shi, F. Qu, Enhanced triethylamine-sensing properties of P-N heterojunction Co₃O₄/In₂O₃ hollow microtubes derived from metal-organic frameworks, *Sensor. Actuator. B Chem.* 262 (2018) 739–749.
- [32] Y. Fang, S.-R. Zhu, M.-K. Wu, W.-N. Zhao, L. Han, MOF-derived In₂S₃ nanorods for photocatalytic removal of dye and antibiotics, *J. Solid State Chem.* 266 (2018) 205–209.
- [33] L.-N. Jin, X.-Y. Qian, J.-G. Wang, H. Aslan, M. Dong, MIL-68 (In) nano-rods for the removal of Congo red dye from aqueous solution, *J. Colloid Interface Sci.* 453 (2015) 270–275.
- [34] T. He, B. Ni, X. Xu, H. Li, H. Lin, W. Yuan, J. Luo, W. Hu, X. Wang, A competitive coordination strategy to finely tune pore environment of zirconium-based metal-organic frameworks, *ACS Appl. Mater. Interfaces* 9 (2017) 22732–22738.
- [35] T. He, X. Xu, B. Ni, H. Wang, Y. Long, W. Hu, X. Wang, Fast and scalable synthesis of uniform zirconium, hafnium-based metal-organic framework nanocrystals, *Nanoscale* 9 (2017) 19209–19215.
- [36] C. Volkringer, M. Medouri, T. Loiseau, N. Guillo, J. Marrot, G. Ferey, M. Haouas, F. Taulelle, N. Audebrand, M. Latroche, The Kagomé topology of the gallium and indium metal-organic framework types with a MIL-68 structure: synthesis, XRD, solid-state NMR characterizations, and hydrogen adsorption, *Inorg. Chem.* 47 (2008) 11892–11901.
- [37] S. Hermes, T. Witte, T. Hikov, D. Zacher, S. Bahnüller, G. Langstein, K. Huber, R.A. Fischer, Trapping metal-organic framework nanocrystals: an in-situ time-resolved light scattering study on the crystal growth of MOF-5 in solution, *J. Am. Chem. Soc.* 129 (2007) 5324–5325.
- [38] H. Guo, Y. Zhu, S. Wang, S. Su, L. Zhou, H. Zhang, Combining coordination modulation with acid-base adjustment for the control over size of metal-organic frameworks, *Chem. Mater.* 24 (2012) 444–450.
- [39] L.-N. Li, Q. Liu, W.-Y. Sun, Size-controlled indium(III)-benzenedicarboxylate hexagonal rods and their transformation to In₂O₃ hollow structures, *CrysTEngComm* 15 (2013) 4779–4784.
- [40] H. Wang, M. Li, Q. Lu, Y. Cen, Y. Zhang, S. Yao, A mesoporous rod-like g-C₃N₅ synthesized by salt-guided strategy: as a superior photocatalyst for degradation of organic pollutant, *ACS Sustain. Chem. Eng.* 7 (2019) 625–631.
- [41] P. Cai, H. Song, Y. Lv, Hierarchical spheres In₂S₃-based cataluminescence sensor for ammonium sulfide, *Microchem. J.* 138 (2018) 116–121.
- [42] J. Chen, W. Liu, W. Gao, Tuning photocatalytic activity of In₂S₃ broadband spectrum photocatalyst based on morphology, *Appl. Surf. Sci.* 368 (2016) 288–297.
- [43] D.-D. Chen, X.-H. Yi, C. Zhao, P. Wang, C.-C. Wang, Polyaniline modified MIL-100(Fe) for enhanced photocatalytic Cr(VI) reduction and tetracycline degradation under simulated sunlight, *Chemosphere* 245 (2020), 125659.
- [44] C. Zhao, Z. Wang, X. Li, X. Yi, H. Chu, X. Chen, C.-C. Wang, Facile fabrication of BUC-21/Bi₂₄O₃₁Br₁₀ composites for enhanced photocatalytic Cr(VI) reduction under simulated sunlight, *Chem. Eng. J.* 389 (2020), 123431.
- [45] X. Du, X. Yi, P. Wang, J. Deng, C.-c. Wang, Enhanced photocatalytic Cr(VI) reduction and diclofenac sodium degradation under simulated sunlight irradiation over MIL-100(Fe)/g-C₃N₄ heterojunctions, *Chin. J. Catal.* 40 (2019) 70–79.
- [46] Y.-X. Li, H. Fu, P. Wang, C. Zhao, W. Liu, C.-C. Wang, Porous tube-like ZnS derived from rod-like ZIF-L for photocatalytic Cr(VI) reduction and organic pollutants degradation, *Environ. Pollut.* 256 (2020), 113417.
- [47] J. Qiu, M. Li, L. Yang, J. Yao, Facile construction of three-dimensional netted ZnIn₂S₄ by cellulose nanofibrils for efficiently photocatalytic reduction of Cr(VI), *Chem. Eng. J.* 375 (2019), 121990.
- [48] J. Qiu, M. Li, J. Xu, X.-F. Zhang, J. Yao, Bismuth sulfide bridged hierarchical Bi₂S₃/BiOCl/ZnIn₂S₄ for efficient photocatalytic Cr(VI) reduction, *J. Hazard Mater.* 389 (2020), 121858.
- [49] F. Deng, X. Lu, Y. Luo, J. Wang, W. Che, R. Yang, X. Luo, S. Luo, D.D. Dionysiou, Novel visible-light-driven direct Z-scheme CdS/CuInS₂ nanoplates for excellent photocatalytic degradation performance and highly-efficient Cr (VI) reduction, *Chem. Eng. J.* 361 (2019) 1451–1461.
- [50] D. Yang, X. Zhao, X. Zou, Z. Zhou, Z. Jiang, Removing Cr (VI) in water via visible-light photocatalytic reduction over Cr-doped SrTiO₃ nanoplates, *Chemosphere* 215 (2019), 586e595.
- [51] R. Liang, R. Huang, X. Wang, S. Ying, G. Yan, L. Wu, Functionalized MIL-68(In) for the photocatalytic treatment of Cr(VI)-containing simulation wastewater: electronic effects of ligand substitution, *Appl. Surf. Sci.* 464 (2019) 396–403.
- [52] F. Zhang, Y. Zhang, G. Zhang, Z. Yang, D.D. Dionysiou, A. Zhu, Exceptional synergistic enhancement of the photocatalytic activity of SnS₂ by coupling with polyaniline and N-doped reduced graphene oxide, *Appl. Catal. B Environ.* 236 (2018) 53–63.
- [53] J.-C. Wang, J. Ren, H.-C. Yao, L. Zhang, J.-S. Wang, S.-Q. Zang, L.-F. Han, Z.-J. Li, Synergistic photocatalysis of Cr(VI) reduction and 4-Chlorophenol degradation over hydroxylated α -Fe₂O₃ under visible light irradiation, *J. Hazard Mater.* 311 (2016) 11–19.
- [54] X. Hu, W. Wang, G. Xie, H. Wang, X. Tan, Q. Jin, D. Zhou, Y. Zhao, Ternary assembly of g-C₃N₄/graphene oxide sheets/BiFeO₃ heterojunction with enhanced photoreduction of Cr(VI) under visible-light irradiation, *Chemosphere* 216 (2019) 733–741.
- [55] G. Dong, L. Zhang, Synthesis and enhanced Cr(VI) photoreduction property of formate anion containing graphitic carbon nitride, *J. Phys. Chem. C* 117 (2013) 4062–4068.
- [56] Y. Lin, S. Wu, X. Li, X. Wu, C. Yang, G. Zeng, Y. Peng, Q. Zhou, L. Lu, Microstructure and performance of Z-scheme photocatalyst of silver phosphate modified by MWCNTs and Cr-doped SrTiO₃ for malachite green degradation, *Appl. Catal. B Environ.* 227 (2018) 557–570.
- [57] L. Jiang, X. Yuan, G. Zeng, J. Liang, X. Chen, H. Yu, H. Wang, Z. Wu, J. Zhang, T. Xiong, In-situ synthesis of direct solid-state dual Z-scheme WO₃/g-C₃N₄/Bi₂O₃ photocatalyst for the degradation of refractory pollutant, *Appl. Catal. B Environ.* 227 (2018) 376–385.
- [58] T. Cai, W. Zeng, Y. Liu, L. Wang, W. Dong, H. Chen, X. Xia, A promising inorganic-organic Z-scheme photocatalyst Ag₃PO₄/PDI supermolecule with

- enhanced photoactivity and photostability for environmental remediation, *Appl. Catal. B Environ.* 163 (2020), 118327.
- [59] J. Xu, C. Liu, J. Niu, M. Chen, Preparation of In_2S_3 nanosheets decorated KNbO_3 nanocubes composite photocatalysts with significantly enhanced activity under visible light irradiation, *Separ. Purif. Technol.* 230 (2020), 115861.
- [60] J. Lim, H. Kim, J. Park, G.-H. Moon, J.J.M. Vequizo, A. Yamakata, J. Lee, W. Choi, How g- C_3N_4 works and is different from TiO_2 as an environmental photocatalyst: mechanistic view, *Environ. Sci. Technol.* 54 (2020) 497–506.